JOC The Journal of Organic Chemistry

pubs.acs.org/joc Article

Electron Push−Pull Effects on Intramolecular Charge Transfer in Perylene-Based Donor−Acceptor Compounds

Mina Ahn, Min-Ji Kim, Dae Won Cho,* and Kyung-Ryang Wee*

Cite This: https://dx.doi.org/10.1021/acs.joc.0c02149 Read Online

ACCESS | Metrics & More | Article Recommendations | SI Supporting Information

ABSTRACT: A series of asymmetric donor−acceptor (D−A) perylene-based compounds, 3-(*N*,*N*-bis(4′-(R)-phenyl)amino)perylene (**Peri−DPA(R)**), were successfully prepared to explore their intramolecular charge transfer (ICT) properties. To induce ICT between the donor and acceptor, diphenylamine (DPA) derivatives (electron donor units) with the same functional groups (**R** = CN, F, H, Me, or OMe) at both para positions were linked to the C-3 position of perylene to produce five **Peri−DPA** derivatives. A steady-state spectroscopy study on **Peri−DPA(R)**s exhibited a progressively regulated ICT trend consistent with the substituent effect as it progressed from the electron-withdrawing group to the electron-donating group. In particular, a comparative study using a D−A−D (donor−acceptor−donor) system demonstrated that not only the electron push−pull substituent effect but also subunit combinations influence photophysical and electrochemical properties. The different ICT characters observed in Lippert−Mataga plots of **D−A(CN)** and **D−A−D(CN)** (CN-substituted **D−A** and **D−A−D**) led to the investigation on whether ICT emission of two systems with differences in subunit combinations is of the same type or of a different type. The femtosecond transient absorption (fs-TA) spectroscopic results provided direct evidence of ICT origin and confirmed that **D−A(CN)** and **D−A−D(CN)** exhibited the same transition mix of ICT (from donor to acceptor) and reverse ICT (rICT, from arylamine to CN unit). Density functional theory (DFT)/TD-DFT calculations support the presence of ICT for all five compounds, and the experimental observations of rICT presented only for CN-substituted compounds.

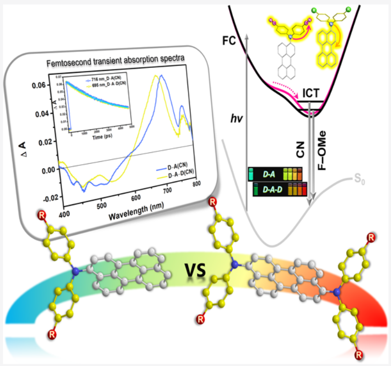

■ INTRODUCTION

Donor−acceptor molecules containing dipolar organic chromophores exhibiting intramolecular charge transfer (ICT) are a class of functional π-conjugated organic systems, which are useful tunable molecules in the solar energy conversion and storage,[1,2] molecular electronic,[3−5] photovoltaic,[6−8] photoeletrochemical cell (PEC),[9] and light-emitting diode[10−12] fields. ICT generally occurs in push−pull molecular systems containing an electron donor (D) and an electron acceptor (A).[13−16] Various push−pull molecules are known to have small band gaps and relatively strong dipoles, which contribute to efficient ICT.[17,18] The ICT character of a D−A system is critical in terms of its optical and electronic properties[19−21] and can be controlled by using suitable combinations of the donor and acceptor components.[22,23] Also, combinations of D and A strongly affect frontier orbital levels, and thus, can be used to tune the optoelectronic properties.[17]

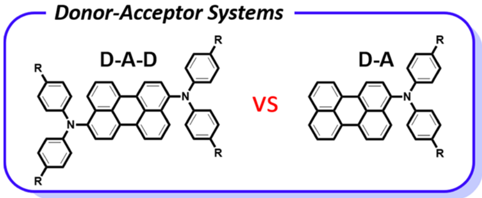

Recently, our group reported the ICT properties on the perylene-based donor−acceptor−donor (D−A−D) system with regard to the electron push−pull substituent effect.[24] Specifically, good linear correlations between photophysical properties and Hammett substituent constants showed that all perylene-based D−A−D compounds with electron-withdrawing and donating R groups (R = CN, F, H, Me, and OMe) followed the same ICT trend. In addition, the ICT properties of these systems were systematically controlled by donor modulation, which allowed emission colors to be effectively tuned. However, in Lippert−Mataga plots, a different charge-transfer character was observed for the CN-substituted perylene-based D−A−D compound. As a result, we suggested that emission color tuning for the D−A−D molecular system is limited in terms of generating high-energy blue emission due to reverse ICT (rICT) from arylamine to CN unit caused by the presence of a strong electron-withdrawing group. In this report, along the line of the study, we carefully investigated the

Received: September 6, 2020

Scheme 1. Synthetic Route to Peri–DPA(R)[a]

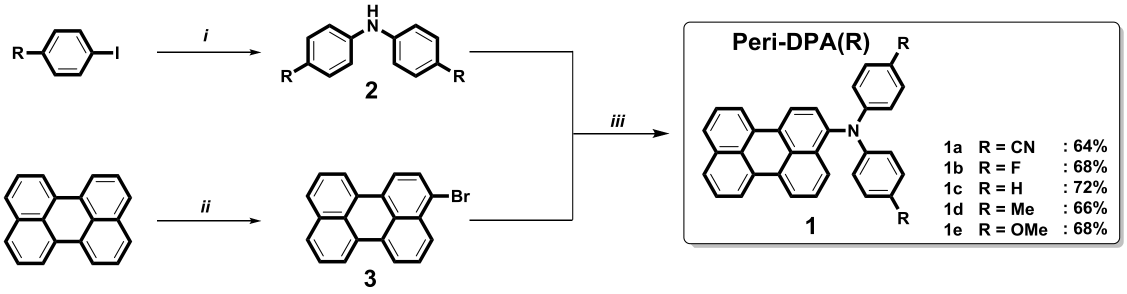

[a]Reagents and conditions: (i) CuI, $LiNH_2$, K_3PO_4, DMF, reflux, 24 h. (ii) NBS, anhydrous tetrahydrofuran (THF), 24 h, r.t. (iii) $Pd(dba)_3$, Xantphos, NaO*t*-Bu, toluene, reflux, 24 h.

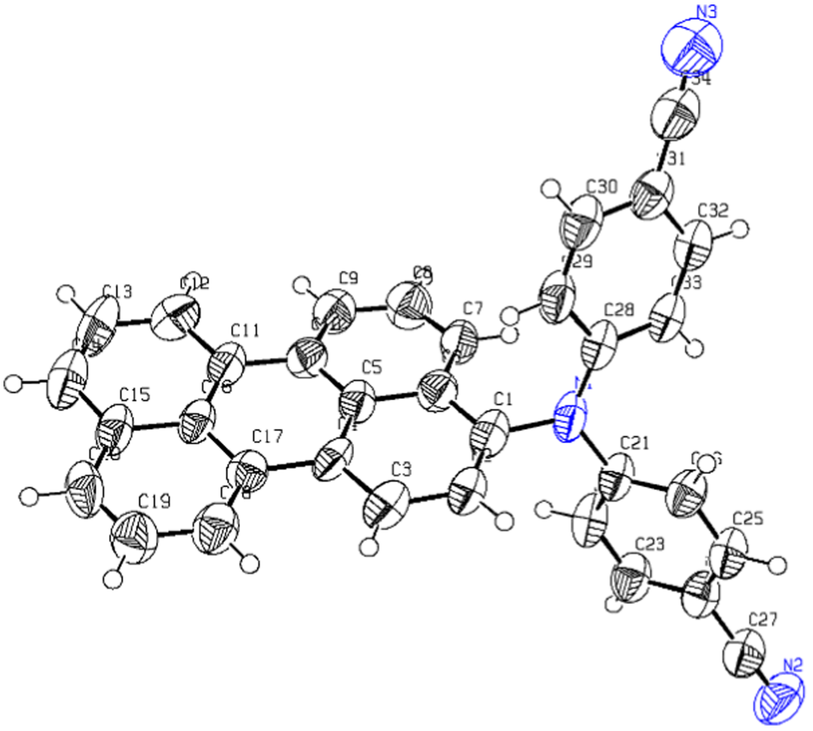

Figure 1. ORTEP drawings of compound **1a**. Ellipsoid contour percent probability level is 50%.

electron push–pull effects of substituents in a perylene-based D–A system with a particular focus on ICT and rICT.

To allow comparisons with our previous study on a D–A–D system, we prepared an asymmetric D–A molecular structure, similar to the D–A–D system using diphenylamine (DPA) derivatives as electron donors and perylene as the electron acceptor. The electron-rich diphenylamine (DPA) is widely used as a functional group to facilitate electron donor and/or hole transport properties.[25−28] On the other hand, perylene derivatives have been intensively investigated as functional materials in optoelectronics due to their chemical, thermal, and photochemical stabilities,[29,30] high fluorescence quantum yields,[31,32] and planar geometries.[33,34] Given the symmetry of perylene, the attachment of the donor or acceptor subunit in the same direction as the direction of ICT intensifies the oscillator strength and increases the absorption capacity.[35] Therefore, we selected a series of well-conjugated perylene D–A molecules by connecting DPA at 3-position, an active site on the perylene core.[36−39] In addition, to simplify the comparison, identical substituents were introduced at the para positions of *N*,*N*-diphenylamine.

Although the ICT properties for various D–A and D–A–D derivatives have been investigated, however, molecular structure–property relationship studies that have compared the ICT properties of analogous perylene-based D–A and D–A–D molecular systems are limited.[40,41] In the present study, we aimed to investigate and compare how push–pull substituent influences ICT properties in perylene-based D–A and D–A–D systems. The photophysical ICT properties of both systems were compared and analyzed using steady-state and time-resolved optical spectroscopy. The optical absorption spectroscopic and electrochemical properties confirmed that highest-energy occupied molecular orbital–lowest-energy unoccupied molecular orbital (HOMO–LUMO) gaps were modulated by the introduction of substituents, showing that the D–A system with one DPA substituent had a larger gap than the D–A–D system with two DPA substituents. With regard to energy band-gap control, the optical emission spectroscopic properties showed a wider color tuning range with larger width variation by substituents, for the D–A system than the D–A–D system. In particular, steady-state spectroscopic results in various solvents showed that the dipole moments of molecules affected by substituents varies with the subunit combinations, which may lead to differences in the type of ICT emission control between the two systems. Furthermore, femtosecond transient absorption (fs-TA) spectroscopic results demonstrated that the origins of emissions in D−A and D−A−D systems, even in systems containing the CN unit (**D−A(CN)** and **D−A−D(CN)**), were identical.

■ RESULTS AND DISCUSSION

Synthesis. The target perylene-based D−A compounds (**Peri−DPA(R)**s), 3-(*p*-(R)-diphenylamino)perylene (**1**) (R: CN (**1a**), F (**1b**), H (**1c**), Me (**1d**), and OMe (**1e**)), were synthesized as outlined in Scheme 1. Donor precursors, *p*-(R)-diphenylamine (**2**) (R: CN (**2a**), F (**2b**), H (**2c**), Me (**2d**), and OMe (**2e**)) with the same electron-donating or -withdrawing group at the para-positions of diphenylamines, were prepared according to the previously reported procedures.[50] The acceptor precursor, 3-bromoperylene (**3**), was prepared by the bromination using *N*-bromosuccinimide (NBS). Perylene-based D−A compounds were successfully synthesized by Pd-catalyzed Buchwald amination between 1 molar ratio of *p*-(R)-diphenylamine (**2**) and 3-bromoperylene (**3**). Specifically, the five 3-(*p*-(R)-diphenylamino)perylenes (**1a**−**1e**) were prepared in the presence of 5 mol % $Pd_2(dba)_3$ using Xantphos as a catalyst and excess amounts of NaO*t*-Bu as a base; they were obtained as a yellow or orange solid in the toluene solvent with a yield of 64−72%. All five compounds were purified by silica gel column chromatography using hexane/dichloromethane mixtures as eluents and were further purified by recrystallization. The molecular structures of all of the compounds were determined by ^{1}H and ^{13}C{^{1}H} NMR (Figures S1−S10), elemental analysis, and mass spectrometry (Figure S11). Finally, the structure of **1a** was authenticated by single-crystal X-ray crystallography. The Experimental Section and the Supporting Information (SI) provide detailed synthetic procedures and characterization data.

A single crystal of **1a** was grown by slow evaporation from a CH_2Cl_2/hexane mixture (1:2 v/v) at room temperature (RT), and analyzed by single-crystal X-ray diffraction (XRD) crystallography using synchrotron radiation. Compound **1a** crystallized in the monoclinic space group $P2_1/n$; crystal data and collection parameters are summarized in Tables S1 and S2. Figures 1, S12, and S13 show Oak Ridge thermal ellipsoid plot (ORTEP) drawings and packing of **1a**, respectively. In the packing diagram (Figure S13), **1a** molecules were stacked in a herringbone fashion[42] without face-to-face $\pi-\pi$ overlap between perylene cores. As shown in Figure 1, the two para-substituted phenyl rings in **1a** were twisted in different directions with respect to the perylene core at angles of 45.0(6)° (C1−N1−C21−C22) and 16.5(6)° (C1−N1−C28−C29), which was consistent with that obtained by density functional theory (DFT) optimization of ground-state geometry.

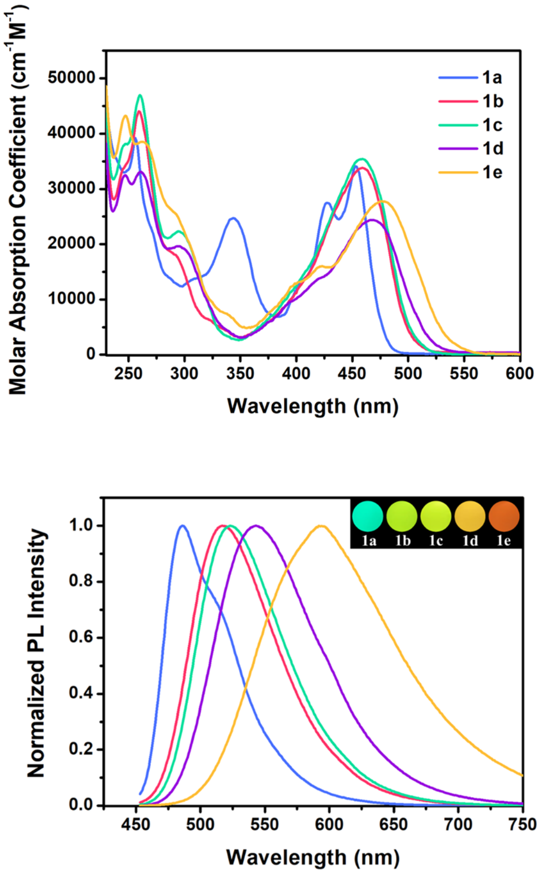

Figure 2. UV−vis absorption (top) and emission (bottom) spectra: **1a** (blue), **1b** (red), **1c** (green), **1d** (purple), **1e** (orange) in CH_2Cl_2 at 10 μM.

Photophysical Properties. Steady-state optical absorption and emission spectra of the five **Peri−DPA(R)**s were measured both in solution (Figure 2) and in solid state (Figure S18), and the spectral parameters are summarized in Table 1. As shown in Figure 2 (top), the spectrum of each compound exhibited two types of absorption bands, that is, high-energy absorption at 250−350 nm and low-energy absorption at 400−525 nm. Absorption vibronic structures at 250−350 nm correspond to the $S_0 \rightarrow {}^1$LE transitions of the diphenylamine (DPA) and perylene moieties, respectively. This transition explicitly shows characteristic absorbances of each subunit of the perylene core $S_0 \rightarrow S_2$ excitation and the DPA series, while maintaining its intrinsic spectral shape, as shown in Figures S14 and S15. A broad, structureless band at 400−525 nm corresponds to the $S_0 \rightarrow {}^1$CT transition, which showed the presence of an intramolecular interaction in the ground state regarding electronic coupling between the DPA and perylene units. As was expected based on considerations of substituent effects, red shift of the CT band followed the order **1a** < **1b** < **1c** < **1d** < **1e**. In particular, the CT band of **1a** exhibited a structured peak similar to $S_0 \rightarrow S_1$ excitation of the perylene core (vibration energy of 1441 cm^{-1}) (Figure S16) because the strong electron-withdrawing ability of the CN unit caused weak electronic coupling with the perylene unit.

As compared with the D−A−D system, the D−A system showed a shorter wavelength range and a smaller shift in the absorption maxima wavelength (Figure S20 top), indicating the reduced conjugation length and relatively weak energy control by fewer DPA substituents in the ground state. Moreover, the structured CT band of **1a** was more clearly observed in the D−A system than in the D−A−D system (Figure S17), which showed that the asymmetric D−A system retains the electronic structure of perylene itself, while the symmetric D−A−D system loses some of the electronic structure of perylene itself. For this reason, the properties of subunits were more prominent in the D−A system than in the D−A−D system. Regarding intermolecular interactions, thin-film absorption and emission spectra of **1a**−**1e** (Figure S18)

Table 1. Photophysical Properties of **1a**−**1e**

	λ_{max}abs (nm)	λ_{max}PL(nm)		Φ_f[c]				
compd	sol[a]/film[b]	sol[a]/film[b]	Stokes shift (cm^{-1})	sol[a]	τ_F[d] (ns)	k_{rad}[e] × 10^7 (s^{-1})	k_{nr}[e] × 10^7 (s^{-1})	k_{rad}/k_{nr}
1a	453/472	486/560	1499	0.60	4.076	14.7	9.83	1.50
1b	459/482	517/549	3012	0.58	6.368	9.11	6.59	1.38
1c	459/483	523/567	3377	0.54	6.616	8.16	6.95	1.17
1d	468/492	543/570	3747	0.55	9.058	6.07	4.97	1.22
1e	476/512	592/599	5034	0.17	6.467	2.63	12.8	0.20

[a] Absorption and emission maximum for the lowest energy band in CH_2Cl_2 at room temperature (RT). [b] Measured in thin films. [c] Fluorescence quantum yields, with 9,10-diphenylanthracene (Φ_{PL} = 0.95, ethanol) as the standard, in CH_2Cl_2 at RT. [d] Fluorescence lifetime in CH_2Cl_2. [e] Values of k_{rad} and k_{nr} were calculated using $k_{rad} = \Phi_f/\tau_F$ and $k_{nr} = (1/\tau_F) - k_{rad}$.

were found to exhibit red shifts as compared with spectra obtained in hexane, which suggested that as was observed in the D−A−D system, the D−A system also forms J-aggregates.

The fluorescence properties of the **Peri−DPA(R)**s in CH_2Cl_2 solutions were studied and compared. As was observed for maximum absorption, emission maxima were greatly influenced by substituents. The emission maxima of the **Peri−DPA(R)**s are in the range of 486−592 nm for systematic red shifts and the extended spectral bandwidth (Figure 2, bottom). The emission spectrum of **1a** had a structured peak as observed in the CT absorption spectrum (Figures 2 and S20 left), indicating a small structural change between the ground and excited states. In other words, unlike other members of the **Peri−DPA(R)**, the excited state of **1a** retained some of the characteristics of the ground state, due to a strong electron-withdrawing effect of the CN unit. In addition, as shown in Table 1 and Figure S21, depending on the substituent effect, the increase in Stokes shifts, that is, 1499 cm^{-1} for **1a**, 3012 cm^{-1} for **1b**, 3377 cm^{-1} for **1c**, 3747 cm^{-1} for **1d**, and 5034 cm^{-1} for **1e**, was observed, indicating an increase in the CT character in the excited state. The fluorescence quantum yields (Φ_f) of **Peri−DPA(R)**s showed a gradual decrease of 17−60% as the electron-donating power of substituents increased. Fluorescence lifetimes varied from 4 to 10 ns in CH_2Cl_2, and all fluorescence decay profiles showed exponential decay, suggestive of radiative decay from a single excited state (Figure S19). Using the Φ_f and τ_F values of **Peri−DPA(R)s**, the radiative and nonradiative decay rate constants (k_{rad} and k_{nr}) were calculated and determined in the range of ∼10^7. From the electron-withdrawing group (EWG) to the electron-donating group (EDGs) substitution, the k_{rad} values gradually decreased, while the k_{nr} value did not show a gradual increase (Table 1). These results show that the k_{rad} values are controlled by the electron push−pull substituent effects that influence the typical single CT emission band.

Considering the above-mentioned results on the D−A system, the CT emission properties of D−A and D−A−D subunit combinations were compared. The D−A system showed a slightly larger shift range of maximum emission wavelengths than the D−A−D system (Figure S20 bottom), which shows a relatively wider energy control range by substituents in the excited state caused by more polarization of the asymmetric D−A system. In both systems, the spectral shift intervals were broader in the excited states than in the ground states, but the degrees of change in shift intervals between the ground and excited states were significantly greater in the D−A system (Figure S20), which was ascribed to charge delocalization in the symmetric D−A−D system and relatively more localization in the asymmetric D−A system than in the D−A−D system. For the same substituents, the D−A system exhibited a larger Stokes shift than the D−A−D system (Figure S21), leading to lower Φ_f and longer τ_F values, which was caused by structural flexibility due to greater reorganization energy in the excited state. However, for CN unit substitution, Stokes shifts in the D−A−D system were larger (Figure S21). This is due to rICT from arylamine to the CN unit by strong EWG ability of the CN unit as well as ICT from DPA donor to perylene acceptor, which means that the polarization region was expanded by ICT and rICT, in the delocalization D−A−D system; as a result, the larger Stokes shifts in the **D−A−D(CN)** was observed.

Solvatochromic Properties. The absorption and emission behaviors of the **Peri−DPA(R)**s in different solvents were investigated to study the solvatochromic effect (Table S3, Figures S22, and S23). Generally, D−A molecules exhibiting ICT are more solvated in the excited state than in the ground state.[43,44] As was expected, more significant red shifts were observed in the emission spectra than in the absorption spectra (Figures S22 and S23), due to stabilization of the more polarized emitting state by polar solvents. In particular, the solvatochromic shift in the emission spectra gradually increased from EWGs to EDGs, indicating that the **Peri−DPA(R)**s well demonstrated the substituent effect. To quantitatively estimate the experimental dipole moment changes between the ground and excited states, Stokes shifts ($\Delta\nu$) of compounds **1a**−**1e** were plotted as a function of solvent polarity parameters (Δf), according to the Lippert−Mataga method using eq 1

$$\begin{aligned}\Delta\nu = \overline{\nu_a} - \overline{\nu_f} &= \frac{2}{hca_0^3}\left(\frac{\varepsilon - 1}{2\varepsilon + 1} + \frac{n^2 - 1}{2n^2 + 1}\right) \times (\mu_e - \mu_g)^2 + \text{constant} \\ &= 2\Delta f \times \frac{\Delta\mu^2}{hca_0^3} + \text{constant}\end{aligned} \quad (1)$$

where $\mu_e - \mu_g$ ($\Delta\mu$) is the difference between the dipole moments in the excited and ground states, c is the speed of light, h is Planck's constant, and a_0 is the radius of the Onsager cavity around the fluorophore. The dielectric constants (ε) (1.9 *n*-hexane, 2.02 cyclohexane, 2.38 toluene, 7.6 THF, 9.1 CH_2Cl_2, and 37.5 CH_3CN) and the refractive indices (n) of solvents are included in the term Δf, which is known as orientation polarizability. Onsager radii, obtained using B3LYP/6-31G, were considered to be half the average size for **1a**−**1e**, that is, 16.0, 14.6, 14.4, 15.6, and 16.2 Å, respectively. Using the slopes in eq 1, increments in dipole moment changes ($\Delta\mu$) for **1a**−**1e** were estimated to be 11.6, 16.8, 17.0, 21.9, and 26.7 D, respectively. Table S4 shows the values of the ground-state dipole moment (μ_g) obtained by the DFT method for energy-minimized structures. These were >0 due to the asymmetries of these compounds (7.0 D for **1a**, 1.8 D for **1b**, 0.2 D for **1c**, 0.4 D for **1d**, and 0.4 D for **1e**). From ground-state dipole moments (μ_g) and dipole moment changes ($\Delta\mu$), excited-state dipole moments (μ_g) were calculated to be 18.6 D for **1a**, 18.6 D for **1b**, 17.2 D for **1c**, 22.3 D for **1d**, and 27.2 D for **1e**. As EWGs and EDGs in the D−A system are substituted, μ_g and μ_e values became large. The largest μ_g value was the CN-substituted **1a**, and the largest μ_e value was the OMe-substituted **1e**. In particular, **1a** substituted with strong EWGs showed the largest μ_g value among the **Peri−DPA(R)**s. However, μ_e was relatively small and this led to the smallest $\Delta\mu$ value for **1a**. As was observed for the D−A system, the μ_g and μ_e values of the D−A−D system were affected by the electron push−pull substituent effect and showed the same trend as values of the D−A system. As shown in Table S5, for CN-substituted compounds, the μ_g and μ_e values were relatively large for substituent series in the D−A−D system. Due to the molecular symmetry of the D−A−D system, the μ_g value was close to 0, and thus, the relatively large μ_e value affected the $\Delta\mu$ value. D−A and D−A−D systems with the same substituents were compared (Tables S4 and S5), and it was found that the μ_g, μ_e, and $\Delta\mu$ values of the D−A system were mostly greater than those of the D−A−D system. However, for CN-substituted compounds, the μ_e and $\Delta\mu$ values of the D−A−D system were larger than the D−A system. For the CN-substituted D−A−D system, expansion of the polarization region by ICT and rICT and the more expanded polarization region due to an increase in donor subunits increased μ_e and $\Delta\mu$ values in the D−A−D system more than those in the D−A system.

As shown in Figures 3 and S24, the Lippert−Mataga plot for the D−A system showed a linear correlation with solvent polarity and followed a substituent effect on its slope. The slope of the fitting line from EWGs to EDGs increased steadily in proportion to $(\Delta\mu)^2$ in the order **1a** < **1b** < **1c** < **1d** < **1e**, which resulted in an effective ICT control. In contrast, in the D−A−D system, the Lippert−Mataga plot was not entirely consistent with the substituent effect (Figure S25), due to the relatively large $\Delta\mu$ value of **D−A−D(CN)**. In addition, comparing **D−A(CN)** and **D−A−D(CN)** a discrepancy in the slope tendencies of Lippert−Mataga plots indicated that the ICT properties of these CN-substituted compounds depend on subunit combinations. In particular, the exceptional slope tendency observed for **D−A−D(CN)** showed notable ICT properties, which distinguished it from other D−A−Ds. More specifically, for **D−A−D(CN)**, we suggest the additional rICT property from the arylamine to the CN unit, along with the ICT property common to all D−A−D series. Of these two ICT properties, rICT, which was observed only in **D−A−D(CN)**, was ascribed to the strong electron-withdrawing effect of the CN unit within DPA substituents. Considering the area where rICT occurs, **D−A(CN)** with the same DPA substituent could also cause rICT like **D−A−D(CN)**. Based on the above results, it is unclear whether **D−A(CN)** and **D−A−D(CN)** have identical ICT origins.

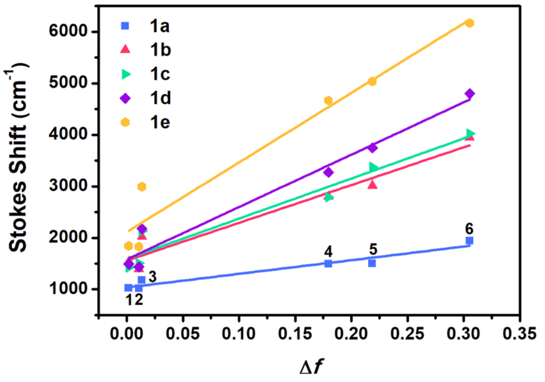

Figure 3. Lippert−Mataga plots for **1a**−**1e** in different solvents: 1, *n*-hexane; 2, cyclohexane; 3, toluene; 4, THF; 5, CH_2Cl_2; 6, CH_3CN.

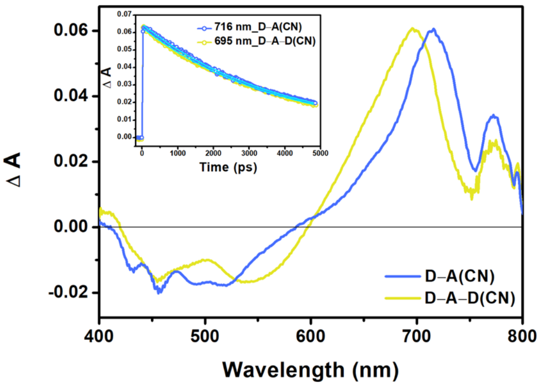

Figure 4. Transient absorption spectra of **D−A(CN)** and **D−A−D(CN)** in CH_2Cl_2 solution. The excitation wavelength was 350 nm. Inset: decay profiles were monitored at selected wavelengths.

Femtosecond Transient Absorption (fs-TA) Measurements. To determine whether ICT origins differed for **D−A(CN)** and **D−A−D(CN)** and between D−A and D−A−D systems containing other functional groups, femtosecond transient absorption (fs-TA) measurements were performed in CH_2Cl_2 using laser excitation at 350 nm. The TA spectra exhibited a strong excited-state absorption (ESA) band at 600−800 nm and a negative band at 460−550 nm (Figures 4 and S28), and spectral shapes were not changed at different time delays (Figure S26). Imran et al.[39] reported that the strong positive ESA band in the range 600−750 nm is attributed to the $S_1 \rightarrow S_n$ transition of perylene and the negative band at ∼440 nm corresponds to the ground-state bleaching (GSB) and the stimulated emission (SE) of perylene. Based on the steady-state spectroscopic result, the negative TA band in the range 460−550 nm is attributed to the GSA and SE, and the strong positive TA bands in the 600−800 nm region are attributed to the ICT state than to the $S_1 \rightarrow S_n$ transition for all perylene-based D−A and D−A−D systems including **D−A(CN)** and **D−A−D(CN)**. The transient absorption spectra between D−A and D−A−D systems are qualitatively similar, suggesting that D−A−D system, including **D−A−D(CN)**, indirectly can behave as a D−A system due to the symmetry breaking in the excited state (Figure S28).[45,46] For fs-TA spectra of longer wavelength (600−800 nm), D−A and D−A−D systems were divided into a broad, intense band at 600−750 nm and a shoulder band at 750−800 nm. The broad TA band at 600−750 nm showed a spectral shift by substituents with a larger shift interval for the D−A system than for the D−A−D system (Figure S28), due to the large polarization of the asymmetric system. In addition, the weak TA band at 750−800 nm was also affected by substituents, and intensity changes by substituents were greater for the D−A system than for the D−A−D system (Figure S28). In particular, unlike that observed for other substituents, both **D−A(CN)** and **D−A−D(CN)** exhibited a distinctive TA band at 750−800 nm (Figure 4). Based on TA spectral comparisons, we believe that the emission origin of **D−A(CN)** and **D−A−D(CN)** differed from that of other members of the D−A and D−A−D series.

Decay profiles were analyzed to investigate the excited-state kinetics of D−A and D−A−D. As was expected, on a picosecond time scale, similar decay patterns were observed for the respective systems (inset in Figure S28), except for those containing the CN unit (Figure S27). **D−A(CN)** and **D−A−D(CN)** were observed with a long time scale (≈5 ns) for a clear comparison between the two (inset in Figure 4). Measured on a long time scale, the time profile of **D−A−D(CN)** monitored at 695 nm was fitted as the lifetime of 3.75 ± 0.06 ns, and the time profile of **D−A(CN)** monitored at 716 nm was fitted as the lifetime of 3.74 ± 0.07 ns. This consistency between the TA spectra of **D−A(CN)** and **D−A−D(CN)** was attributed to similar ICT properties. On the other hand, at 772 nm, new TA peaks decayed with a lifetime of 2.90 ± 0.3 and 3.98 ± 0.1 ns for **D−A−D(CN)** and **D−A(CN)**, respectively. These decay times were different from that observed at ESA maxima wavelengths of 695 and 716 nm, respectively. This means that for both **D−A(CN)** and **D−A−D(CN)**, the overall TA spectral behavior appeared to be mixed with an emission origin other than the ICT mentioned above. In a previous report on **D−A−D(CN)**, its unique transition origin was demonstrated using steady-state spectroscopic and calculation results, and this uniqueness was assumed to be due to rICT from the arylamine to the CN unit. Although the steady-state spectroscopic results of **D−A(CN)** and **D−A−D(CN)** did not delineate with certainty whether the two CN-substituted compounds had the same or different origins, transient absorption measurements clearly indicated that emission origins were similar. In conclusion, unlike members of the D−A and D−A−D series with one ICT origin, both **D−A(CN)** and **D−A−D(CN)** had in common a transition mix of ICT and rICT.

In combination with the above-mentioned results, the ICT emission origin for perylene based D−A and D−A−D systems can be summarized as follows as shown in Figure 5. All D−A and D−A−D systems upon ultrafast excitation indicated dynamics involved in transition from Franck−Condon (FC) state to ICT state, where the ICT occur from arylamine to perylene unit. The observed TA spectra showed the red-shift as the EDG ability increased, which means that this ICT state was stabilized, and it is in agreement with the electron push−pull substituent effect. In particular, by comparing the TA spectra and decay profile, we suggest that both **D−A(CN)** and **D−A−D(CN)** mixed with an emission origin from arylamine to CN unit, different from ICT mentioned above, as well as the ICT. Therefore, perylene-based D−A and D−A−D systems indicated the ICT process was in good agreement with the electron push−pull substituent effect, but **D−A(CN)** and **D−A−D(CN)** occurred the additional emission origin by strong EWG ability of CN unit. As a result, F−OMe unit of D−A and D−A−D system showed one ICT origin from DPA donor to perylene acceptor, while CN unit of D−A and D−A−D system showed mixture of the emission origin, ICT and rICT (from arylamine to CN unit).

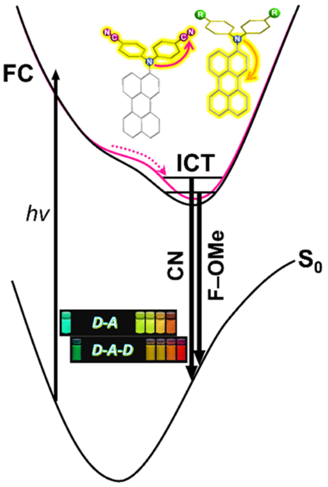

Figure 5. Schematic potential curves for D−A and D−A−D systems. pink line: **D−A(CN)** and **D−A−D(CN)**; black line: **D−A(F−OMe)** and **D−A−D(F−OMe)**.

Electrochemical Properties. Cyclic voltammetry (CV) of the **Peri−DPA** series was performed in 1 mM CH_2Cl_2 solution containing n-Bu_4NClO_4 (0.1 M) as a supporting electrolyte to investigate redox properties and energy levels (Figure S29). HOMO/LUMO energy levels were determined using oxidation onset potentials and electronic spectral data (summarized in Table 2 and Figure S30). All five compounds showed only one reversible oxidation wave and no reduction wave. The first oxidation onset potentials ($E_{\text{onset}}^{\text{ox}}$) were determined to be 0.89 V for **1a**, 0.74 V for **1b**, 0.72 V for **1c**, 0.65 V for **1d**, and 0.58 V for **1e**, which can be explained by the stabilities of the cationic species generated from the **Peri−DPA** unit. As electron-donating propensities of the DPA substituents increased, the **Peri−DPA** unit is first oxidized and its unstable oxidized species is compensated by the effective π-conjugation. Furthermore, the introduction of a substituent influences the experimental and calculated E_{HOMO} and E_{LUMO} values, which was −5.53 ± 0.17 and −3.08 ± 0.02 for experimental values and −4.87 ± 0.48 and −2.05 ± 0.38 for calculated values. As shown in Figure S31, E_{HOMO} values were more affected by the electron push−pull substituent effect than the E_{LUMO} values. In particular, the experimentally estimated E_{LUMO} values were similar for all five compounds due to the same perylene acceptor, which indicated that the electron acceptor was largely unaffected by the electron donor at the LUMO level.

The optical band gaps ($E_{\text{g}}^{\text{opt}}$) from absorption edges were determined to be 2.60, 2.48, 2.47, 2.39, and 2.31 eV for **1a−1e**, respectively, that is, band gaps widened on increasing the electron-withdrawing character of substituents. The theoretical band gaps ($\text{E}_{\text{g}}^{\text{cal}}$) from DFT calculations for **1a−1e** were determined to be 2.92, 2.82, 2.82, 2.77, and 2.67 eV, respectively and this trend agreed well with optical band gaps. For the D−A−D molecules previously reported, a similar trend to the D−A system was observed between band gaps and substituent effects. In addition, when comparing the effects of one and two donors with the same substituent type, one-donor systems had larger optical and theoretical energy band gaps (Figure S32). This indicates that in both D−A and D−A−D systems, electronic communication occurs between the DPA nitrogen and perylene and is affected by the substituents through the π-conjunction system of the phenyl linked to the

Table 2. Energy Band-Gap Properties of **1a**−**1e**

	experimental			calculated		
compd	HOMO[a] (eV)	LUMO[b] (eV)	E_g^{opt} (eV)	HOMO[c] (eV)	LUMO[c] (eV)	E_g^{cal} (eV)
1a	−5.70[d] (−6.00[e])	−3.10	2.60	−5.35	−2.43	2.92
1b	−5.54[d] (−5.85[e])	−3.06	2.48	−4.87	−2.05	2.82
1c	−5.53[d] (−5.83[e])	−3.06	2.47	−4.78	−1.96	2.82
1d	−5.46[d] (−5.76[e])	−3.07	2.39	−4.68	−1.91	2.77
1e	−5.39[d] (−5.69[e])	−3.08	2.31	−4.53	−1.86	2.67

[a] E_{HOMO} (eV) = $-e(E_{onset}^{ox} + 4.8)$. [b] E_{LUMO} (eV) = $-e(E_{HOMO} + E_g^{opt})$. [c] Obtained by the DFT calculation. [d] Estimated assuming that the HOMO energy of ferrocene lies 4.80 eV below the vacuum level.[47] [e] Estimated assuming that the HOMO energy of ferrocene is −5.11 eV in CH_2Cl_2.[48]

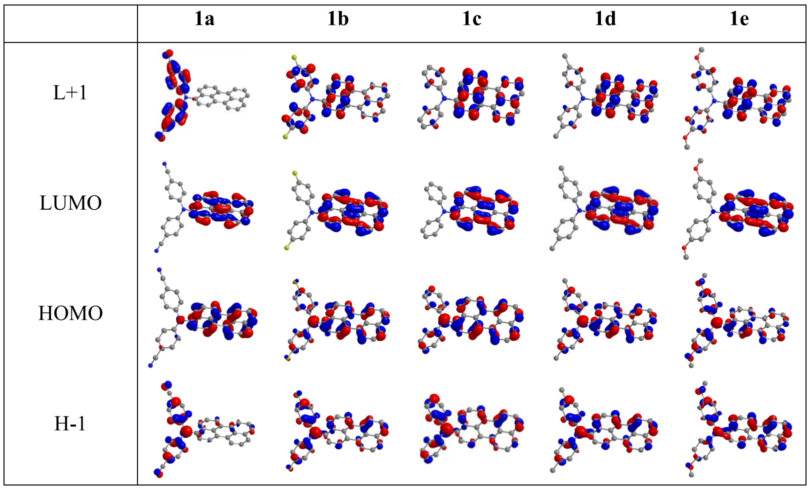

Figure 6. Frontier orbital distributions (HOMO − 1, HOMO, LUMO, LUMO + 1) of **1a**−**1e** calculated by the DFT using the B3LYP function and 6-31G(d,p) basis.

N atom. These results show that band gaps are predictable based on considering the substituent effect and subunit composition.

Density Functional Theory (DFT). To gain deeper understanding of the geometric and electronic properties of the target molecules, density functional theory (DFT) calculations and time-dependent DFT (TD-DFT) calculations were conducted using the Gaussian 16 program. Geometric optimization was performed in the gas phase at the B3LYP/6-31G(d,p) level. The B3LYP DFT method provided sufficiently reliable qualitative insights rather than quantitative analysis of experimental results. The frontier orbital distributions of **1a**−**1e** estimated from DFT calculations are depicted in Figure 6. HOMO-1, HOMO, and LUMO+1 molecular orbitals, but not LUMOs, were influenced by substituents. HOMO orbitals of **1a**−**1e** were delocalized over perylene and DPA moieties, and distribution in the two phenyls of DPA increased on increasing electron donation. The H-1 orbitals of **1a**−**1e** were delocalized over DPA and perylene moieties, which is expanded from DPA moiety to perylene moiety as the electron-donating character of substituents increases. However, LUMO orbitals of **1a**−**1e** were localized on the perylene moiety, whereas L + 1 orbital distribution decreased in the two phenyl groups of DPA and increased in the perylene, as the electron-donating propensity increases. Unlike the other four compounds, the molecular orbitals of **1a** were highly localized on either perylene or DPA, which is attributed to the weak electronic coupling between donor and acceptor.

Considering the results of TD-DFT calculations (B3LYP/6-31G) shown in Figures S38−S42 and Tables S12−S16, all five compounds demonstrated a major charge-transfer transition from an amino-delocalized HOMO to a perylene-localized LUMO, due to efficient HOMO/LUMO overlap on the perylene core. In addition, transitions from the diarylamino-delocalized H-1 to the perylene-localized LUMO and from the amino-delocalized HOMO to the diarylperylene-delocalized L + 1 were minor charge-transfer transitions. In contrast to the other compounds, for **1a**, the strong electron-withdrawing ability of the CN unit facilitated the transition from the HOMO to L + 1 at ca 412 nm rather than from H-1 to the LUMO. In our previous study on the D−A−D system, we reported that additional rICT, a minor transition from the HOMO to L + 1 at ca 372 nm can occur within the DPA moiety due to the strong electron-withdrawing character of the CN unit. Likewise, in the D−A system, a similar phenomenon was observed, which means that in D−A−D and D−A systems, strong electron-withdrawal and vulnerable HOMO/L + 1 overlap cause a weak electronic coupling between the donor and acceptor. In addition, the D−A−D system, which possesses an added donor subunit as compared with the D−A system, is relatively favorable for rICT due to enhanced ICT in the two donor components. Summarizing, for both D−A−D and D−A systems, ICT is mainly controlled by the electronic transition from HOMOs to LUMOs, and the rICT seen only in the CN-substituted compounds was observed in both D−A and D−A−D systems.

■ CONCLUSIONS

Along the line of the perylene-based donor−acceptor−donor (D−A−D) system, the donor−acceptor (D−A) system, **Peri−DPA(R)** (**1a−1e**), were designed and synthesized by modifying only a subunit combination under the same substituent conditions. To investigate the influence of the electron push−pull substituent effect on ICT control, the photophysical and electrochemical properties of the five **Peri−DPA(R)**s were examined and compared to those of the D−A−D system. Steady-state spectroscopic results of **Peri−DPA(R)**s showed predictable ICT properties in that the D−A system was in good agreement with the substituent effect. In particular, Lippert−Mataga plots for the D−A system demonstrated systematic ICT control by substituents, which differed from that observed for the D−A−D system. Comparisons of the D−A and D−A−D systems for each substituent suggested that different slope tendencies in Lippert−Mataga plots of **D−A(CN)** and **D−A−D(CN)** were caused by different emission origins. However, considering that both have the same subunits required for ICT and rICT formation, the same emission origin for **D−A(CN)** and **D−A−D(CN)** was also suggested. The femtosecond transient absorption (fs-TA) spectroscopic results confirmed that emissions of **D−A(CN)** and **D−A−D(CN)** were from the same origin based on ICT and rICT. In addition, DFT calculations supported the notion that ICT and rICT exist only for CN-substituted compounds regardless of subunit combination. The results presented in this study are helpful in designing D−A molecules for efficient ICT and understanding its fundamental structure−property relationship.

■ EXPERIMENTAL SECTION

General. Based on the standard Schlenk techniques, all of the synthesis experimental procedures were performed under a dry argon condition. Reagents and solvents were purchased from commercial sources and used as received without further purification, unless otherwise stated. All reactions were monitored with thin-layer chromatography (TLC) using commercial TLC plates (Merck Co.). Silica gel column chromatography was performed on silica gel 60 G (230−400 mesh ASTM, Merck Co.). The synthesized compounds were characterized by ^{1}H NMR or ^{13}C{^{1}H} NMR and elemental analysis. The ^{1}H and proton-decoupled ^{13}C spectra were recorded on a Bruker500 spectrometer operating at 500 and 125 MHz, respectively, and all proton and carbon chemical shifts were measured relative to the internal residual chloroform (99.5% $CDCl_3$) from the lock solvent. The elemental analyses (C, H, N, O) were performed using a Thermo Fisher Scientific Flash 2000 series analyzer. The GC-MS analysis was performed using a highly sensitive gas chromatograph/mass selective detector spectrometer (Agilent, 7890B-5977B GC/MSD). The 3-bromoperylene[49] and *p*-(R)-diphenylamine[50] were prepared based on the previously published method. The crystal structure was determined by single-crystal X-ray diffractometer at the Western Seoul Center of Korea Basic Science Institute.

Synthesis of Peri−DPA(R) (1). A mixture of 3-bromoperylene (0.46 g, 1.39 mmol), *p*-(R)-diphenylamine (1.46 mmol, R: CN (**2a**), F (2b), H (**2c**), Me (**2d**), and OMe (**2e**)), sodium *tert*-butoxide (0.96 g, 10 mmol), Xantphos (0.04 g, 5 mol %), $Pd_2(dba)_3$ (0.06 g, 5 mol %) in toluene (30 mL) was refluxed under an argon atmosphere at 110 °C via a heating mantle overnight. After the reaction mixture was cooled to room temperature (RT), deionized water (40 mL) was poured, and organic layer was separated using a separating funnel. The water layer was washed using methylene chloride (×3) for the extracted remaining organic residue. After combining all of the organic solvents, the organic layer was dried over anhydrous $MgSO_4$ and then filtered off. The solvent was removed under reduced pressure, and the residue was purified with column chromatography (silica gel, CH_2Cl_2/hexane mixture eluent). Finally, 3-(*p*-(R)-diphenylamino)perylene compounds were further purified by using hexane hot filter washing.

Peri−DPA(CN) (1a) 3-(N,N-Bis(4′-cyanophenyl)amino)perylene. Yield: 0.42 g, 64%, orange powder. Eluent (DCM/hexane = 2:1). ^{1}H NMR (500 MHz, $CDCl_3$, ppm) δ 8.26−8.22 (m, 4H), 7.79−7.77 (m, 2H), 7.57−7.53 (m, 7H), 7.45 (t, *J* = 7.5 Hz, 1H), 7.36 (d, *J* = 8.0 Hz, 1H), 7.18 (d, *J* = 9.0 Hz, 4H). ^{13}C{^{1}H} NMR (125 MHz, $CDCl_3$, ppm) δ 150.0 (2C), 139.7, 134.6, 133.7 (4C), 132.5, 132.0, 131.8, 130.6, 130.6, 130.5, 130.2, 128.8, 128.6, 128.5, 128.4, 128.1, 126.8, 126.7, 122.4, 121.5 (4C), 121.1, 121.0 (2C), 120.6, 119.0, 105.6 (2C). anal. calcd for $C_{34}H_{19}N_3$: C, 86.97; H, 4.08; N, 8.95. found: C, 86.74; H, 4.11; N, 8.87. GC-MS (*m*/*z*) calcd: 469.53; found: 469.2

Peri−DPA(F) (1b) 3-(N,N-Bis(4′-fluorophenyl)amino)perylene. Yield: 0.43 g, 68%, yellow powder. Eluent (DCM/hexane = 1:4). ^{1}H NMR (500 MHz, $CDCl_3$, ppm) δ 8.12−8.05 (m, 4H), 7.68 (d, *J* = 8.0 Hz, 1H), 7.61 (t, *J* = 8.0 Hz, 2H), 7.40 (td, *J* = 8.0, 2.5 Hz, 2H), 7.29 (t, *J* = 7.5 Hz, 1H), 7.15 (d, *J* = 8.0 Hz, 1H), 6.94−6.90 (m, 4H), 6.84 (t, *J* = 8.0 Hz, 4H). ^{13}C{^{1}H} NMR (125 MHz, $CDCl_3$, ppm) δ 159.2, 157.3, 144.7 (2C), 143.3, 134.7, 131.9, 131.8, 131.1, 130.9, 130.5, 129.4, 128.5, 128.1, 127.8, 127.0 (2C), 126.7, 123.9, 123.4 (4C), 120.8, 120.7, 120.5, 120.2, 116.1 (4C), 115.9. anal. calcd for $C_{32}H_{19}F_2N$: C, 84.38; H, 4.20; N, 3.08. found: C, 84.40; H, 4.11; N, 3.18. GC-MS (*m*/*z*) calcd: 455.50; found: 455.1

Peri−DPA(H) (1c) 3-(N,N-Diphenylamino)perylene. Yield: 0.42 g, 72%, yellow powder. Eluent (DCM/hexane = 1:4). ^{1}H NMR (500 MHz, $CDCl_3$, ppm) δ 8.11−8.06 (m, 4H), 7.72 (d, *J* = 8.0 Hz, 1H), 7.72 (dd, *J* = 5.5, 2.5 Hz, 2H), 7.40 (t, *J* = 7.5 Hz, 2H), 7.27 (t, *J* = 8.0 Hz, 1H), 7.23 (d, *J* = 8.0 Hz, 1H), 7.14 (t, *J* = 8.0 Hz, 4H), 7.01 (d, *J* = 8.5 Hz, 4H), 6.88 (t, *J* = 7.0 Hz, 2H). ^{13}C{^{1}H} NMR (125 MHz, $CDCl_3$, ppm) δ 148.2 (2C), 143.3, 134.7, 132.2, 131.8, 131.2, 131.0, 130.4, 129.5, 129.4, 129.2 (4C), 128.5, 127.9, 127.8, 127.7, 127.0 (2C), 126.6, 124.2, 122.0 (4C), 121.9, 120.9, 120.6, 120.4, 120.2. anal. calcd for $C_{32}H_{21}N$: C, 91.62; H, 5.05; N, 3.34. found: C, 91.60; H, 5.12; N, 3.28. GC-MS (*m*/*z*) calcd: 419.52; found: 419.2

Peri−DPA(Me) (1d) 3-(N,N-Bis(4′-methylphenyl)amino)-perylene. Yield: 0.41 g, 66%, yellow powder. Eluent (DCM/hexane = 1:4). ^{1}H NMR (500 MHz, $CDCl_3$, ppm) δ 8.10−8.04 (m, 4H), 7.73 (d, *J* = 8.0 Hz, 1H), 7.59 (t, *J* = 8.0 Hz, 2H), 7.39 (td, *J* = 8.0, 2.5 Hz, 2H), 7.27 (t, *J* = 8.0 Hz, 1H), 7.18 (d, *J* = 8.0 Hz, 1H), 6.94 (d, *J* = 8.0 Hz, 4H), 6.88 (d, *J* = 8.5 Hz, 4H), 2.21 (s, 6H). ^{13}C{^{1}H} NMR (125 MHz, $CDCl_3$, ppm) δ 146.2 (2C), 143.9, 134.7, 132.1, 131.7, 131.3, 131.2 (2C), 131.1, 130.4, 129.8 (4C), 128.9, 128.5, 127.9, 127.5, 127.3, 126.8, 126.6, 126.6, 124.4, 122.1 (4C), 120.9, 120.6, 120.3, 120.0, 20.7 (2C). anal. calcd for $C_{34}H_{25}N$: C, 91.24; H, 5.63; N, 3.13. found: C, 91.74; H, 5.21; N, 3.05. GC-MS (*m*/*z*) calcd: 447.57; found: 447.3

Peri−DPA(OMe) (1e) 3-(N,N-Bis(4′-methoxyphenyl)amino)-perylene. Yield: 0.45 g, 68%, orange powder. Eluent (DCM/hexane = 1:1). ^{1}H NMR (500 MHz, $CDCl_3$, ppm) δ 8.20−8.13 (m, 4H), 7.85 (d, *J* = 8.5 Hz, 1H), 7.69 (t, *J* = 8.5 Hz, 2H), 7.49 (td, *J* = 8.0, 3.5 Hz, 2H), 7.36 (t, *J* = 8.0 Hz, 1H), 7.23 (d, *J* = 8.0 Hz, 1H), 7.00 (d, *J* = 9.0 Hz, 4H), 6.80 (d, *J* = 9.0 Hz, 4H), 3.79 (s, 6H). ^{13}C{^{1}H} NMR (125 MHz, $CDCl_3$, ppm) δ 154.8 (2C), 144.4, 142.6, 134.7, 131.7, 131.6, 131.3, 131.2, 130.4, 128.5, 128.4, 127.8, 127.4, 126.6 (2C), 126.6, 126.5, 126.4, 124.5, 123.6 (4C), 120.9, 120.5, 120.2, 119.9, 114.6 (4C), 55.5 (2C). anal. calcd for $C_{34}H_{25}NO_2$: C, 85.15; H, 5.25; N, 2.92. found: C, 85.34; H, 5.16; N, 2.88. GC-MS (*m*/*z*) calcd: 479.57; found: 479.2

Preparation of Single Crystal 1a. For the crystallization of compound **1a**, a vacuum-dried pure sample of **1a** was taken in a vial and dissolved in 1:2 dichloromethane/hexane mixed solvent. Slow evaporation of the solvent at room temperature for one month yielded the orange needle-shaped crystal. Then the crystals were picked up from the vial and a single-crystal XRD study was performed.

X-ray Crystal Structure Analysis. The preliminary examination and data collection were performed using a Bruker SMART CCD detector system single-crystal X-ray diffractometer equipped with a sealed-tube X-ray source (50 kV × 30 mA) using graphite-monochromated Mo Kα radiation (λ = 0.71073 Å). Preliminary unit cell constants were determined using a set of 45 narrow-frame (0.3° in ω) scans. The double-pass method of scanning was used to exclude noise. Collected frames were integrated using an orientation matrix determined from narrow-frame scans. The SMART software package was used for data collection, and SAINT was used for frame integration.[51] Final cell constants were determined by global refinement of the xyz centroids of reflections harvested from the entire data set. Structure solution and refinement were carried out using the SHELXTL-PLUS software package.[52]

Spectroscopic Measurements. The UV−vis absorption spectra were recorded using a Sinco Mega-2100 spectrophotometer in the dual-beam mode, and the fluorescence emission measurements were carried out using a Shimadzu fluorometer (RF-6000) with a wavelength resolution of ∼1 nm. Fluorescence lifetimes were measured by PicoQuant FluoTime 200 that takes advantage of the time-correlated single photon counting method. A pulsed diode laser operated at 20 MHz repetition rate was used as the excitation source. The FWHM of a laser pulse was typically 45 ps, and the instrument response function was ∼190 ps when the Hamamatzu photomultiplier tube (H5783-01) was used. The emission quantum yields (Φ_{PL}) were calculated using William's comparative method for samples of five different concentrations of (1−10) μM, using 9,10-diphenylanthracene (Φ_{PL} = 0.95, ethanol) as a reference standard.[53]

The sub-picosecond time-resolved absorption spectra were collected using a pump−probe transient absorption spectroscopy system (Ultrafast Systems, Helios). The pump light was generated using a regenerative amplified titanium sapphire laser system (Spectra Physics, Spitfire Ace, 1 kHz) pumped by a diode-pumped Q-switched laser (Spectra Physics, Empower). The seed pulse was generated using a titanium sapphire laser (Spectra Physics, MaiTai SP). The pulses (350 nm) generated from an optical parametric amplifier (Spectra Physics, TOPAS prime) were used as the excitation pulse. Further, a white light continuum pulse, which was generated by focusing the residual of the fundamental light to a thin Sapphire crystal after the controlled optical delay, was used as a probe beam and directed to the sample cell with 2.0 mm of the optical path and detected with a CCD detector installed in the absorption spectroscope. The pump pulse was chopped by the mechanical chopper synchronized to one-half of the laser repetition rate, resulting in a pair of the spectra with and without the pump, from which the absorption change induced by the pump pulse was estimated.

Cyclic Voltammetry (CV). A CH Instruments 701D potentiostat was used for electrochemical measurements, and cyclic voltammetry (CV) was performed in an electrolytic solution prepared using 1 mM of electroactive compounds and 0.1 M tetrabutyl ammonium perchlorate (NBu_4ClO_4) in deoxygenated dichloromethane. A three-electrode configuration, glassy carbon, platinum wire, and saturated calomel electrode (SCE), were used as working, counter, and reference electrodes, respectively.

Density Functional Theory Calculations. Density functional theory (DFT) calculations were performed using the Gaussian'16 software package. Full geometry optimizations in their ground state were performed using the B3LYP functional and the 6-31G(d,p) basis set for all atoms. The excitation energies and oscillator strengths for the lowest 100 singlet−singlet transitions at the optimized geometry in the ground state were obtained in time-dependent DFT (TD-DFT) calculations using the same basis set and functional as for the ground state. All isodensity plots of the frontier orbitals were visualized by Chem3D Ultra and GaussView software. More detailed DFT/TD-DFT calculation results for 3-(*p*-(R)-diphenylamino)perylenes are described in the SI.

■ ASSOCIATED CONTENT

Supporting Information

The Supporting Information is available free of charge at https://pubs.acs.org/doi/10.1021/acs.joc.0c02149.

> NMR spectra; GC−MS data; X-ray crystallography; absorption spectra of DPA donor, perylene acceptor, and D−A compounds; comparison of photophysical properties of D−A and D−A−D systems; absorption, and emission spectra in various solvents and in the solid state, emission lifetime profile; Lippert−Mataga plots and dipole moment values of D−A and D−A−D systems; femtosecond transient absorption spectroscopic data; CV, HOMO and LUMO energy levels and Hammett plots; comparison of the energy band gap of D−A and D−A−D systems; and DFT/TD-DFT calculation results; X-ray crystallographic data of compound **1a** (PDF)

Accession Codes

CCDC 2042435 contains the supplementary crystallographic data for this paper. These data can be obtained free of charge via www.ccdc.cam.ac.uk/data_request/cif, or by emailing data_request@ccdc.cam.ac.uk, or by contacting The Cambridge Crystallographic Data Centre, 12 Union Road, Cambridge CB2 1EZ, UK; fax: +44 1223 336033.

■ AUTHOR INFORMATION

Corresponding Authors

Dae Won Cho − *Department of Chemistry, Yeungnam University, Gyeongsan, Gyeongbuk 38541, Republic of Korea;* orcid.org/0000-0001-8000-8413; Email: dwcho00@yu.ac.kr

Kyung-Ryang Wee − *Department of Chemistry and Institute of Natural Science, Daegu University, Gyeongsan 38453, Republic of Korea;* orcid.org/0000-0002-9923-8902; Email: krwee@daegu.ac.kr

Authors

Mina Ahn − *Department of Chemistry and Institute of Natural Science, Daegu University, Gyeongsan 38453, Republic of Korea*

Min-Ji Kim − *Department of Chemistry and Institute of Natural Science, Daegu University, Gyeongsan 38453, Republic of Korea*

Complete contact information is available at: https://pubs.acs.org/10.1021/acs.joc.0c02149

Notes

The authors declare no competing financial interest.

■ ACKNOWLEDGMENTS

This research was supported by the Basic Science Research Program through the National Research Foundation of Korea (NRF-2020R1C1C1009007) and Korea Basic Science Institute (National Research Facilities and Equipment Center) grant, funded by the Ministry of Education (2020R1A6C103A028).

■ REFERENCES

(1) Bullock, J. E.; Carmieli, R.; Mickley, S. M.; Vura-Weis, J.; Wasielewski, M. R. Photoinitiated charge transport through π-stacked electron conduits in supramolecular ordered assemblies of donor−acceptor triads. *J. Am. Chem. Soc.* **2009**, *131*, 11919−11929.

(2) Urbani, M.; Ohkubo, K.; Islam, D. S.; Fukuzumi, S.; Langa, F. Photoinduced Energy and Electron Transfer in Phenylethynyl-Bridged Zinc Porphyrin−Oligothienylenevinylene−C_{60} Ensembles. *Chem. - Eur. J.* **2012**, *18*, 7473−7485.

(3) Guldi, D. M. Putting a positive spin on molecular bridges. *Angew. Chem., Int. Ed.* **2010**, *49*, 7844−7846.

(4) Fan, C.; Zhu, L.; Liu, T.; Jiang, B.; Ma, D.; Qin, J.; Yang, C. Using an organic molecule with low triplet energy as a host in a highly

efficient blue electrophosphorescent device. *Angew. Chem.* **2014**, *126*, 2179−2183.

(5) Mishra, A.; Fischer, M. K.; Bäuerle, P. Metal-free organic dyes for dye-sensitized solar cells: From structure: Property relationships to design rules. *Angew. Chem., Int. Ed.* **2009**, *48*, 2474−2499.

(6) Bottari, G.; de la Torre, G.; Guldi, D. M.; Torres, T. Covalent and noncovalent phthalocyanine−carbon nanostructure systems: synthesis, photoinduced electron transfer, and application to molecular photovoltaics. *Chem. Rev.* **2010**, *110*, 6768−6816.

(7) Chen, C.-H.; Ting, H.-C.; Li, Y.-Z.; Lo, Y.-C.; Sher, P.-H.; Wang, J.-K.; Chiu, T.-L.; Lin, C.-F.; Hsu, I.-S.; Lee, J.-H.; Liu, S.-W.; Wong, K.-T. New D−A−A-Configured Small-Molecule Donors for High-Efficiency Vacuum-Processed Organic Photovoltaics under Ambient Light. *ACS Appl. Mater. Interfaces* **2019**, *11*, 8337−8349.

(8) Gautam, P.; Misra, R.; Siddiqui, S. A.; Sharma, G. D. Unsymmetrical Donor−Acceptor−Acceptor−π−Donor Type Benzothiadiazole-Based Small Molecule for a Solution Processed Bulk Heterojunction Organic Solar Cell. *ACS Appl. Mater. Interfaces* **2015**, *7*, 10283−10292.

(9) Wee, K.-R.; Sherman, B. D.; Brennaman, M. K.; Sheridan, M. V.; Nayak, A.; Alibabaei, L.; Meyer, T. J. An aqueous, organic dye derivatized SnO_2/TiO_2 core/shell photoanode. *J. Mater. Chem. A* **2016**, *4*, 2969−2975.

(10) Hancock, J. M.; Gifford, A. P.; Zhu, Y.; Lou, Y.; Jenekhe, S. A. *n*-Type conjugated oligoquinoline and oligoquinoxaline with triphenylamine endgroups: efficient ambipolar light emitters for device applications. *Chem. Mater.* **2006**, *18*, 4924−4932.

(11) Zhu, M.; Yang, C. Blue fluorescent emitters: design tactics and applications in organic light-emitting diodes. *Chem. Soc. Rev* **2013**, *42*, 4963−4976.

(12) Sharma, C. P.; Gupta, N. M.; Singh, J.; Yadav, R. A. K.; Dubey, D. K.; Rawat, K. S.; Jha, A. K.; Jou, J.-H.; Goel, A. Synthesis of Solution-Processable Donor−Acceptor Pyranone Dyads for White Organic Light-Emitting Devices. *J. Org. Chem.* **2019**, *84*, 7674−7684.

(13) Slama-Schwok, A.; Blanchard-Desce, M.; Lehn, J. Intramolecular charge transfer in donor-acceptor molecules. *J. Phys. Chem. A.* **1990**, *94*, 3894−3902.

(14) Kulkarni, A. P.; Kong, X.; Jenekhe, S. A. High-Performance Organic Light-Emitting Diodes Based on Intramolecular Charge-Transfer Emission from Donor−Acceptor Molecules: Significance of Electron-Donor Strength and Molecular Geometry. *Adv. Funct. Mater.* **2006**, *16*, 1057−1066.

(15) Chen, R.; Zhao, G.; Yang, X.; Jiang, X.; Liu, J.; Tian, H.; Gao, Y.; Liu, X.; Han, K.; Sun, M.; Sun, L. Photoinduced intramolecular charge-transfer state in thiophene-π-conjugated donor−acceptor molecules. *J. Mol. Struct.* **2008**, *876*, 102−109.

(16) Panja, S. K.; Dwivedi, N.; Saha, S. Tuning the intramolecular charge transfer (ICT) process in push−pull systems: effect of nitro groups. *RSC Adv.* **2016**, *6*, 105786−105794.

(17) Zöphel, L.; Beckmann, D.; Enkelmann, V.; Chercka, D.; Rieger, R.; Müllen, K. Asymmetric pyrene derivatives for organic field-effect transistors. *Chem. Commun.* **2011**, *47*, 6960−6962.

(18) Lu, X.; Fan, S.; Wu, J.; Jia, X.; Wang, Z.-S.; Zhou, G. Controlling the charge transfer in D−A−D chromophores based on pyrazine derivatives. *J. Org. Chem.* **2014**, *79*, 6480−6489.

(19) Delmond, S.; Létard, J.-F.; Lapouyade, R.; Rettig, W. Photoinduced intramolecular charge transfer in planar vs. twisted donor-acceptor terphenyls. *J. Photochem. Photobiol., A* **1997**, *105*, 135−148.

(20) Ma, W.; Wu, Y.; Han, J.; Gu, D.; Gan, F. Large three-photon absorption and intramolecular charge transfer of the bis-donor fluorene-based molecules. *J. Mol. Struct.* **2005**, *752*, 9−13.

(21) Kim, M.-J.; Ahn, M.; Shim, J. H.; Wee, K.-R. Terphenyl backbone-based donor−π−acceptor dyads: geometric isomer effects on intramolecular charge transfer. *Phys. Chem. Chem. Phys.* **2020**, *22*, 3370−3378.

(22) Kurata, R.; Ito, A.; Gon, M.; Tanaka, K.; Chujo, Y. Diarylamino- and Diarylboryl-Substituted Donor−Acceptor Pyrene Derivatives: Influence of Substitution Pattern on Their Photophysical Properties. *J. Org. Chem.* **2017**, *82*, 5111−5121.

(23) Uebe, M.; Sakamaki, D.; Ito, A. Electronic and Photophysical Properties of 9,10-Anthrylene-Bridged B-π-N Donor-Acceptor Molecules with Solid-State Emission in the Yellow to Red Region. *ChemPlusChem* **2019**, *84*, 1305−1313.

(24) Ahn, M.; Kim, M.-J.; Wee, K.-R. Electron Push−Pull Effects in 3,9-Bis(*p*-(R)-diphenylamino) perylene and Constraint on Emission Color Tuning. *J. Org. Chem.* **2019**, *84*, 12050−12057.

(25) Liu, C.-L.; Zheng, C.-J.; Liu, X.-K.; Chen, Z.; Yang, J.-P.; Li, F.; Ou, X.-M.; Zhang, X.-H. Multifunctional terpyridine/diphenylamine derivatives as highly efficient blue fluorescent emitters and red phosphorescent hosts. *J. Mater. Chem. C* **2015**, 3, 1068−1076.

(26) Jhulki, S.; Moorthy, J. N. Small molecular hole-transporting materials (HTMs) in organic light-emitting diodes (OLEDs): structural diversity and classification. *J. Mater. Chem. C* **2018**, *6*, 8280−8325.

(27) Lee, H. L.; Lee, K. H.; Lee, J. Y. Indoloindole as a new building block of a hole transport type host for stable operation in phosphorescent organic light-emitting diodes. *J. Mater. Chem. C* **2019**, *7*, 5988−5994.

(28) Zhang, Y.; Zheng, Y.; Wang, B.; Ran, H.; Wang, X.; Hu, J.-Y.; Wang, Q. Diphenylamine/triazine hybrids as bipolar hosts for phosphorescent organic light-emitting diodes. *J. Mater. Chem. C* **2020**, *8*, 4461−4468.

(29) Avlasevich, Y.; Li, C.; Müllen, K. Synthesis and applications of core-enlarged perylene dyes. *J. Mater. Chem.* **2010**, *20*, 3814−3826.

(30) Chen, L.; Li, C.; Müllen, K. Beyond perylene diimides: synthesis, assembly and function of higher rylene chromophores. *J. Mater. Chem. C* **2014**, *2*, 1938−1956.

(31) Dawson, W. R.; Windsor, M. W. Fluorescence yields of aromatic compounds. *J. Phys. Chem. B.* **1968**, *72*, 3251−3260.

(32) Icil, H.; Arslan, E. Synthesis and spectroscopic properties of highly pure perylene fluorescent dyes. *Spectrosc. Lett.* **2001**, *34*, 355−363.

(33) Camerman, A. T.; Trotter, J. The crystal and molecular structure of perylene. *Proc. R. Soc. London, Ser. A* **1964**, *279*, 129−146.

(34) Lin, M.-J.; Jiménez, Á. J.; Burschka, C.; Würthner, F. Bay-substituted perylene bisimide dye with an undistorted planar scaffold and outstanding solid state fluorescence properties. *Chem. Commun.* **2012**, *48*, 12050−12052.

(35) Liu, X.; Xu, Z.; Cole, J. M. Molecular design of uv−vis absorption and emission properties in organic fluorophores: toward larger bathochromic shifts, enhanced molar extinction coefficients, and greater stokes shifts. *J. Phys. Chem. C* **2013**, *117*, 16584−16595.

(36) Toguchi, S.; Morioka, Y.; Ishikawa, H.; Oda, A.; Hasegawa, E. Novel red organic electroluminescent materials including perylene moiety. *Synth. Met.* **2000**, *111*−*112*, 57−61.

(37) Torres, É.; Bogel-Lukasik, R.; Berberan-Santos, M. N.; Höfle, S.; Colsmann, A.; Brites, M. J. *N, N′*-Diaryl-perylene-3, 9-diamine derivatives: synthesis, characterization and electroluminescence properties. *RSC Adv.* **2016**, *6*, 107180−107188.

(38) Li, Y.; Zhu, R.; Wang, J.; Li, Z. S.; Xu, N.; Zhang, J.; Wang, P. *N*-Annulated Perylene-Based Hole Transporters for Perovskite Solar Cells: The Significant Influence of Lateral Substituents. *ChemSusChem* **2018**, *11*, 672−680.

(39) Imran, M.; Sukhanov, A. A.; Wang, Z.; Karatay, A.; Zhao, J.; Mahmood, Z.; Elmali, A.; Voronkova, V. K.; Hayvali, M.; Xing, Y. H.; Weber, S. Electronic coupling and spin−orbit charge-transfer intersystem crossing in phenothiazine−perylene compact electron donor/acceptor dyads. *J. Phys. Chem. C* **2019**, *123*, 7010−7024.

(40) Merz, J.; Steffen, A.; Nitsch, J.; Fink, J.; Schürger, C. B.; Friedrich, A.; Krummenacher, I.; Braunschweig, H.; Moos, M.; Mims, D.; Lambert, C.; Marder, T. B. Synthesis, photophysical and electronic properties of tetra-donor-or acceptor-substituted ortho-perylenes displaying four reversible oxidations or reductions. *Chem. Sci.* **2019**, *10*, 7516−7534.

(41) Merz, J.; Dietrich, L.; Nitsch, J.; Krummenacher, I.; Braunschweig, H.; Moos, M.; Mims, D.; Lambert, C.; Marder, T. B.

Synthesis, Photophysical and Electronic Properties of Mono-, Di-, Tri-Amino-Substituted Ortho-Perylenes, and Comparison to the Tetra-Substituted Derivative. *Chem. - Eur. J.* **2020**, 12050−12059.

(42) Dong, H.; Wang, C.; Hu, W. High performance organic semiconductors for field-effect transistors. *Chem. Commun.* **2010**, *46*, 5211−5222.

(43) Detert, H.; Schmitt, V. Quadrupolar donor−acceptor substituted oligo (phenylenevinylene) s—synthesis and solvatochromism of the fluorescence. *J. Phys. Org. Chem.* **2004**, *17*, 1051−1056.

(44) Clarke, T. M.; Gordon, K. C.; Kwok, W. M.; Phillips, D. L.; Officer, D. L. Tuning from π,π^* to charge-transfer excited states in styryl-substituted terthiophenes:An ultrafast and steady-state emission study. *J. Phys. Chem. A* **2006**, *110*, 7696−7702.

(45) Dereka, B.; Rosspeintner, A.; Li, Z.; Liska, R.; Vauthey, E. Direct visualization of excited-state symmetry breaking using ultrafast time-resolved infrared spectroscopy. *J. Am. Chem. Soc.* **2016**, *138*, 4643−4649.

(46) Beckwith, J. S.; Rosspeintner, A.; Licari, G.; Lunzer, M.; Holzer, B.; Fröhlich, J.; Vauthey, E. Specific monitoring of excited-state symmetry breaking by femtosecond broadband fluorescence upconversion spectroscopy. *J. Phys. Chem. Lett.* **2017**, *8*, 5878−5883.

(47) Pommerehne, J.; Vestweber, H.; Guss, W.; Mahrt, R. F.; Bässler, H.; Porsch, M.; Daub, J. Efficient two layer leds on a polymer blend basis. *Adv. Mater.* **1995**, *7*, 551−554.

(48) Connelly, N. G.; Geiger, W. E. Chemical redox agents for organometallic chemistry. *Chem. Rev.* **1996**, *96*, 877−910.

(49) Torres, É.; Berberan-Santos, M. N.; Brites, M. J. Synthesis, photophysical and electrochemical properties of perylene dyes. *Dyes Pigm.* **2015**, *112*, 298−304.

(50) Tlili, A.; Monnier, F.; Taillefer, M. Selective one-pot synthesis of symmetrical and unsymmetrical di-and triarylamines with a ligandless copper catalytic system. *Chem. Commun.* **2012**, *48*, 6408−6410.

(51) *SMART and SAINT*; Bruker Analytical X-ray Division: Madison, WI, 2002.

(52) Sheldrick, G. M. *SHELXTL-PLUS Software Package*; Bruker Analytical X-ray Division: Madison, WI, 2002.

(53) Morris, J. V.; Mahaney, M. A.; Huber, J. R. Fluorescence quantum yield determinations. 9,10-Diphenylanthracene as a reference standard in different solvents. *J. Phys. Chem. C.* **1976**, *80*, 969−974.